

Synthesis and Characterization of Novel Magnetic Nano-Biocomposite Hydrogels Based on Starch-*g*-poly(acrylic acid) Reinforced by Cellulose Nanofibers for Cu²⁺ Ion Removal

Nasime Mirhoseini Renani, Nasrin Etesami,* and Tayebeh Behzad

Cite This: *ACS Omega* 2023, 8, 21929–21940

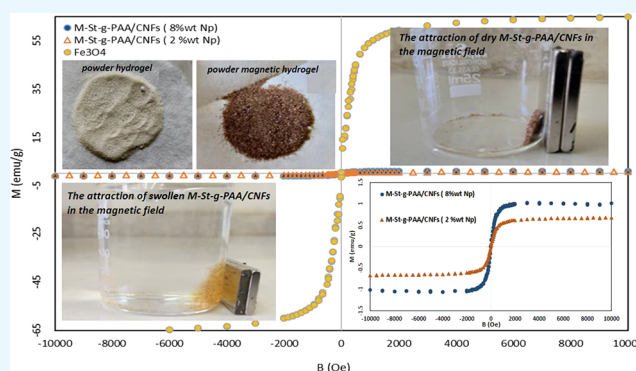
Read Online

ACCESS |

Metrics & More

Article Recommendations

ABSTRACT: One of the crucial challenges of the adsorption process is to recapture the adsorbent from the solution, especially for adsorbents in powder form. This study synthesized a novel magnetic nano-biocomposite hydrogel adsorbent to successfully remove Cu²⁺ ions, followed by convenient recovery and reusability of the adsorbent. The Cu²⁺ adsorption capacity of starch-g-poly(acrylic acid)/cellulose nanofibers (St-g-PAA/CNFs) composite hydrogel and magnetic composite hydrogel (M-St-g-PAA/CNFs) was investigated and compared in both bulk and powder forms. Results showed that Cu²⁺ removal kinetics and swelling rate were improved by grinding the bulk hydrogel into powder form. The kinetic data and adsorption isotherm were best correlated with the pseudo-second-order and Langmuir models, respectively. The maximum monolayer adsorption capacity values of M-St-g-PAA/CNFs hydrogels loaded with 2 and 8 wt % Fe₃O₄ nanoparticles in 600 mg/L Cu²⁺ solution were found to be 333.33 and 555.56 mg/g, respectively, compared to 322.58 mg/g for the St-g-PAA/CNFs hydrogel. Vibrating sample magnetometry (VSM) results demonstrate that the magnetic hydrogel that included 2 and 8 wt % magnetic nanoparticles exhibited paramagnetic behavior with the magnetization of 0.6–0.66 and 1–1.04 emu/g at the plateau, respectively, which showed a proper magnetic property and good magnetic attraction in the magnetic field for separating the adsorbent from the solution. Also, the synthesized compounds were characterized by scanning electron microscopy (SEM), energy dispersive X-ray analysis (EDX), and Fourier transform infrared spectroscopy (FTIR). Finally, the magnetic bioadsorbent was successfully regenerated and reused for four treatment cycles.



1. INTRODUCTION

With the development of modern industry, water pollution by paints and intermediate metals has become a major global problem. Heavy metals and dyes, even in low concentrations, are harmful to microorganisms and aquatic creatures and can also disrupt the normal function of humans and cause various diseases such as cancer. Therefore, reducing or eliminating the heavy metals and dyes in industrial effluents entering the environment and contaminants in the agricultural and food industries is necessary. Common methods for removing heavy metals in water are chemical oxidation, chemical precipitation, ion exchange, filtration, reverse osmosis, bio-removal,^{1,2} solvent extraction, flocculation, and adsorption.³ In recent years, more attention has been focused on using polymeric adsorbents for water treatment due to the high efficiency of the adsorption process, even at low adsorbent concentrations, the simplicity of the adsorption process, and the reusability of the adsorbent.^{4–10} In this regard, biopolymers have attracted a lot of attention due to their biocompatibility, non-toxicity, and natural availability for bioremediation.^{1,2} For example, combining a keratin

biopolymer and a high-surface-area cerium metal–organic framework (Ce-MOF)⁹ and the conversion of inexpensive Cilantro plants (*Coriandrum sativum*) into activated carbon (AC)¹⁰ lead to high-porosity adsorbents that treat dye-contaminated wastewater, which show excellent and rapid removal efficiency.

Many polymers can coordinate with metals or interact with organic compounds, so polymeric-based hydrogels can be used in water treatment. In the meantime, combining minerals such as magnetite nanoparticles with organic polymers is one of the most exciting topics in achieving high-performance adsorbents.^{11–17} Magnetite nanoparticles have superparamagnetic properties, low toxicity, and biocompatibility. The addition of

Received: March 16, 2023

Accepted: May 23, 2023

Published: June 6, 2023



magnetic nanoparticles in the polymer network creates a magnetic hydrogel adsorbent with not only enhanced exposed surface area but also the ability to recover after water treatment due to its magnetic characteristic. Several reports exist in the literature about the synthesis of magnetic nanocomposites, mainly focusing on improving their properties and expanding their use in various applications.^{18–21} Konwar et al.²² synthesized magnetic alginate–Fe₃O₄ hydrogel fibers using a simple laboratory micropipette to absorb an antibiotic. Su et al.²³ investigated the activity of magnetic hydrogel derived from wheat straw cellulose and feather protein as a catalyst for the reduction process of 2-nitrobenzoic acid (2-NA) to 2-amino-benzoic acid (2-ABA). In another research, Zhao et al.²⁴ developed magnetic field-responsive hemicellulose hydrogels for drug delivery. Several studies^{12,25} were conducted to remove dyes and heavy metals with magnetic hydrogels. The Fe₃O₄ nanoparticle content can control the thermal stability, macro/microstructure, swelling behavior, and magnetization of the hybrid hydrogels. The hydrogels can be reinforced by magnetic nanoparticles (MNPs) in two different nanocomposite preparation methods. In the first method, MNPs could be added to monomer suspension during free-radical polymerization and chemically reacted to the polymer matrix, leading to uniform dispersion and distribution of MNPs inside the polymer. In another method, MNPs are added into pre-formed hydrogels and entrapped by physical interlocking.²⁶ Due to the only physical bond between nanoparticles and the hydrogel matrix, the lower stability of the nanoparticles can be achieved in the second method. Therefore, most researchers have preferred synthesizing magnetic hydrogels with the first method,^{20,27–30} and fewer studies were carried out on the second method.²⁶

From previous studies, it can be noticed that hydrogels as superadsorbents have shown a successful performance in heavy metal ion elimination. Although hydrogels in the form of bulks and pieces have a high swelling capacity in waste treatments, however, due to lower surface contact area, their metal ion adsorption capacity is not satisfied. Therefore, in this research, the swelling and adsorption capacity of Cu²⁺ by the starch-g-poly(acrylic acid)/cellulose nanofibers (St-g-PAA/CNFs) composite hydrogel as a reinforced bioadsorbent was examined and compared in both bulk and powder forms. Moreover, the effect of nanomagnetic particle addition on the adsorption behavior of the hydrogel was investigated. Since one of the major challenges of the adsorption method is the adsorbent recovery from the solution, especially in the powder form, the magnetic hydrogel was recovered and reused, and its desorption and re-adsorption capacity was investigated.

2. EXPERIMENTAL SECTION

2.1. Materials. Starch ((C₆H₁₀O₅)_n·(H₂O)), potassium persulfate (K₂SO₄), *N,N'*-methylene bisacrylamide (MBA), acrylic acid (AA), and sodium hydroxide (NaOH) were purchased from Merck, Germany, and characterized by analytical grades. Nano Novin Polymer Co. (Sari, Iran) provided CNFs produced by a chemo-mechanical process from a softwood source. Magnetic nanoparticles (Fe₃O₄) were purchased from Sigma-Aldrich Company. For preparing a Cu²⁺ stock solution with a concentration of 600 ppm, Cu(SO₄)·5H₂O was purchased from Merck Company, Germany.

2.2. Synthesis of the M-St-g-P(AA)/CNFs Hydrogel Bioadsorbent. A general procedure for preparation of the St-g-P(AA)/CNFs composite was conducted as follows: Starch (1.00 g) was added to distilled water (30.00 mL) in a four-necked

reactor equipped with a stirrer (400 rpm). The reactor was placed in a thermostated water bath preset at 85 to 95 °C for 1 h. Then, potassium persulfate (1 wt % with respect to the amount of AA monomer) was added to the solution as the initiator. Afterward, a solution containing 10 mL of distilled water, 1 wt % MBA as the crosslinker, 3.65 g of AA as a monomer, and 2 g of CNFs was gradually poured into the reactor for radical polymerization (75 °C for 3 h). The prepared hydrogels were then completely immersed in an alkaline solution. Unreacted material was eliminated as follows: First, the synthesized hydrogel was immersed in ethanol to replace water. Then, hydrogels were cut into small pieces and merged into distilled water overnight to swell. Afterward, they were again steeped in ethanol to extract all unreacted monomers and extra water molecules following the previous study.³¹ Finally, the resultant hydrogel bulk was placed in an oven to be dried until a constant weight was reached.

To synthesize a magnetic hydrogel, the same procedure was carried out, while Fe₃O₄ nanoparticles (2 and 8 wt % AA monomer content) were added during the synthesis. In this approach, the magnetic nanoparticles were sonicated in the suspension containing a monomer, cellulose nanofibers, and a crosslinker for 10 min, and then the mixture was slowly added to the reaction solution. To compare their ability for metal ion adsorption, hydrogels were prepared in bulk and powder forms. To prepare the hydrogel powder with an average particle size of 0.01 mm, the dried bulk was ground using a high-energy ball mill (Spex-MM950). The synthesis steps of M-St-g-PAA/CNFs are shown in Figure 1.

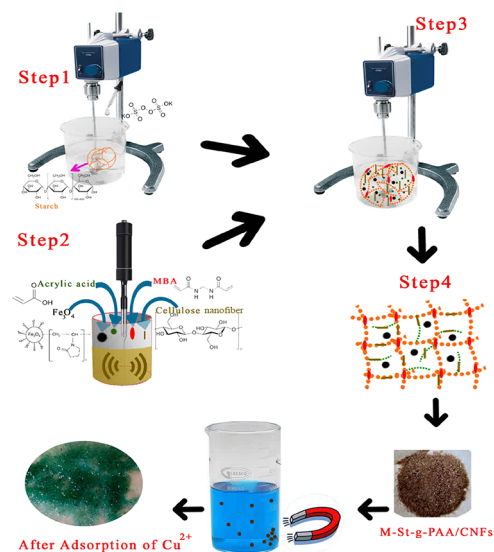


Figure 1. Synthesis steps of M-St-g-PAA/CNFs.

2.3. Characterization of the Synthesized Adsorbents.

To analyze the chemical structure of the synthesized nanocomposite hydrogel adsorbents, FTIR spectroscopy was used. The powdered hydrogel samples were mixed with KBr and then pressed into discs to use for the FTIR spectrometer (Bruker tensor 27, Germany) in the wavelength range from 4000 to 500 cm⁻¹. The morphology structure and elemental changes of the hydrogels before and after the adsorption of Cu²⁺ ions were analyzed using scanning electron microscopy (SEM) images prepared by an FEI Quanta 200 model and EDX analysis. The

magnetic property of the synthesized adsorbent was evaluated using vibrating sample magnetometry (VSM; MDKB).

2.4. Adsorption of Cu²⁺. To study the removal of the Cu²⁺ ions from the aqueous solution by hydrogels, different solutions of Cu²⁺ ions with various concentrations (0.4–0.6 g/L) were employed; 0.05 g of each hydrogel was dipped into 50 mL of every solution at pH = 5 (see Section 3.6). The amount of Cu²⁺ adsorbed by the given amount of nanocomposite hydrogels at 25 °C was calculated according to eq 1. After reaching the equilibrium state and filtering the solutions, the Cu²⁺ ion concentration was measured by a single-beam spectrophotometer (UV–Vis, Shimadzu 240 model, Japan) ($\lambda = 620$ nm). To increase the color intensity of copper solutions and to show better absorption in the visible region with higher precision, we used ammonia solution.³² The ion concentrations for various samples ($R^2 > 0.998$) were obtained through a calibrated curve using the following equation:

$$q = \frac{(C_0 - C_e)V}{m} \quad (1)$$

and the Cu²⁺ removal efficiency percentage was calculated by the following:

$$\% \text{removal} = \frac{(C_0 - C_e)}{C_0} \times 100 \quad (2)$$

where q is the adsorption capacity at equilibrium (mg/g), C_0 and C_e are the initial and equilibrium concentrations of Cu²⁺ (mg/L), respectively, m is the hydrogel weight (g), and V shows the volume of the solution (L).³¹

2.5. Swelling Measurement. To investigate the swelling behavior of the hydrogel, a certain amount of hydrogel was immersed in 50 mL water solution with different pH values (2, 7, and 11) at room temperature, where HCl and NaOH were used to adjust the pH of the solution. At regular time intervals, the swollen gel was taken out from the medium; its weight was measured after removing the excess water with filter paper. The procedure was continued until a constant weight of the swollen gel was achieved. The swelling ratio (S) was calculated using eq 3:

$$S = \frac{W_s - W_d}{W_d} \quad (3)$$

where W_s and W_d are the weights of the swollen and dried hydrogels, respectively.²⁸

Using eq 4, the swelling rate (SR) and equilibrium swelling (S_e) were estimated from the swelling ratio (S) vs time plot.

$$S_t = S_e(1 - e^{-t/\tau}) \quad (4)$$

where S_t (g/g) and S_e (g/g) represent the swelling ratios at time t and equilibrium time, respectively, and τ (min) represents the rate parameter. The swelling rate (SR) (g/(g·min)) for the hydrogel at different pH values was determined by the following equation:

$$\text{SR} = \frac{S_t}{\tau} \quad (5)$$

where S_t (g/g) is the swelling at time τ (min).²⁸

2.6. Adsorption Isotherms. The amount of adsorbed solute by weight of adsorbents was examined by adsorption isotherms for considering a homogeneous or heterogeneous adsorbent surface on an adsorption process of monolayer or multi-layer, or heat or thermodynamic, which is usually analyzed

by Langmuir, Freundlich, and Temkin models by following linear eqs 6–8.^{33,34}

Langmuir isotherm:

$$C_e/q_e = 1/K_1q_{\max} + C_e/q_{\max} \quad (6)$$

where C_e is the copper equilibrium concentration (mg/L), q_e is the amount of adsorbed copper on adsorbent materials (mg/g), q_{\max} is indicated as the maximum amount of copper adsorption on adsorbent materials (mg/g), and K_1 is the adsorption constant (L/mg).

Freundlich isotherm:

$$\log q_e = \log K_F + 1/n(\log C_e) \quad (7)$$

where K_F is the constant of adsorption capacity (L/mg), and $1/n$ is the constant depicting the adsorption intensity.

Temkin isotherm:

$$q_e = RT/b_T(\ln A_T) + RT/b_T(\ln C_e) \quad (8)$$

where R is the universal gas constant (8.314 J/mol), T is the absolute temperature (K), b_T is the constant related to the heat of adsorption (J/mol), and A_T is the equilibrium binding constant corresponding to the maximum binding energy (L/g).

2.7. Adsorption Kinetics. The kinetic adsorptions explain the mechanisms of copper solute sorption on adsorbent materials. Pseudo-first-order eq (PS-I), pseudo-second-order eq (PS-II), Elovich, and intra-particle diffusion models were used to investigate the characteristic constants of sorption of adsorbent materials by following linear eqs 9–12.^{33,35}

Pseudo-first-order (PS-I) model:

$$\ln(q_e - q_t) = \ln q_e - k_1t \quad (9)$$

where q_e is the amount of adsorbed copper on adsorbent materials (mg/g), q_t is the amount of adsorbed copper at time t (mg/g), and k_1 is the pseudo-first-order rate constant (min⁻¹).

Pseudo-second-order (PS-II) model:

$$t/q_t = t/q_e + 1/k_2q_e^2 \quad (10)$$

where k_2 is the pseudo-second-order rate constant ((g/mg)/min).

Elovich model:

$$q_t = (1/\beta)\ln \alpha\beta + (1/\beta)\ln t \quad (11)$$

where α is the initial adsorption rate (mg/g/min), and β is the extent of surface coverage (g/mg). Intra-particle diffusion model:

$$q_t = k_i t^{0.5} + I \quad (12)$$

where k_i is the intra-particle diffusion rate constant (mg/g·min^{0.5}), and I is the constant that gives an idea about the thickness of the boundary layer.

2.8. Desorption and Reusability. The recovery of adsorbed metal ions and the reusability of the adsorbent are essential factors for evaluating biosorbent usage efficiency. Thus, desorption and reusability were also investigated in this study. For this purpose, the hydrogel that adsorbed Cu²⁺ was mixed in 50 mL HCl (0.1 M) solution for 120 min.^{36,37} The adsorption–desorption cycles were repeated three times by using the same adsorbents. The desorption ratio was calculated by eq 13:

$$\text{desorption ratio}(\%) = \frac{C_d V_d}{(C_0 - C_e)V} \times 100 \quad (13)$$

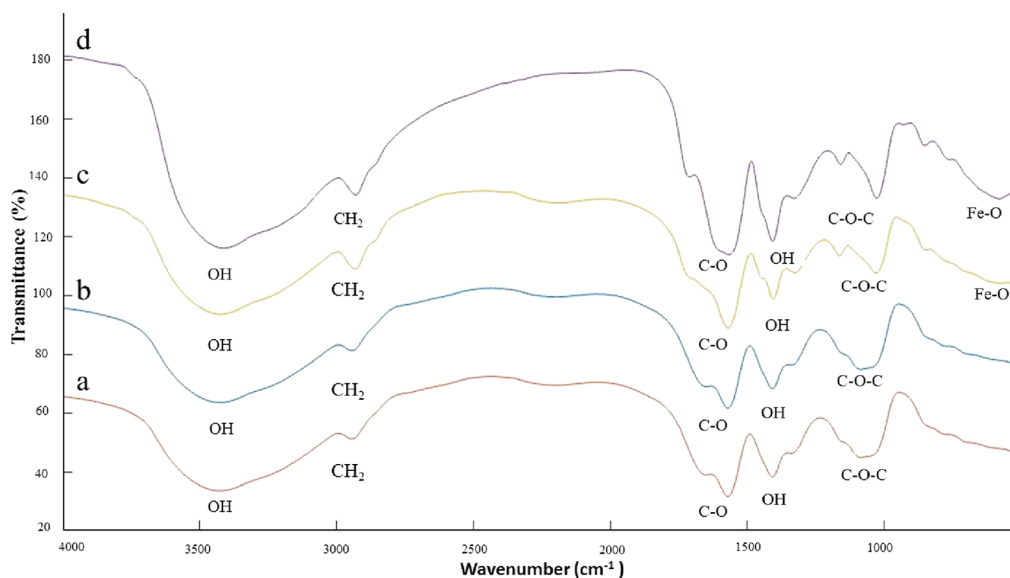


Figure 2. FTIR spectra of (a) St-g-P(AA)/CNFs hydrogels, (b) St-g-P(AA)/CNFs hydrogels after Cu^{2+} adsorption, (c) M-St-g-PAA/CNFs hydrogels, and (d) M-St-g-PAA hydrogels after Cu^{2+} adsorption.

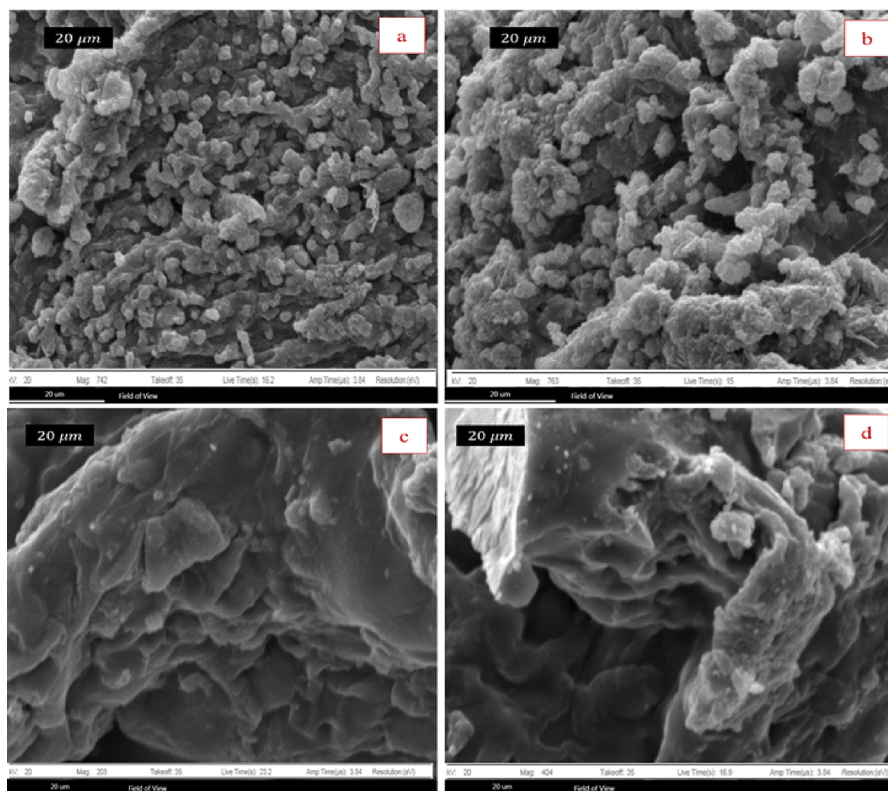


Figure 3. SEM images of (a) St-g-PAA/CNFs and (b) M-St-g-PAA/CNFs before adsorption and (c) St-g-PAA/CNFs and (d) M-St-g-PAA/CNFs after adsorption of Cu^{2+} .

where C_d is the Cu^{2+} concentration in the desorption solutions ($\text{mg}\cdot\text{L}^{-1}$), V_d is the volume of the desorption solution, and V is the volume of the solution.

3. RESULTS AND DISCUSSION

3.1. FTIR Spectroscopy. To explore the intermolecular chemical interactions, such as the formation of hydrogen bonds in the copolymer hydrogel starch-g-poly(acrylic acid) and magnetic starch-g-poly(acrylic acid) in nanocomposite hydro-

gels, FTIR spectroscopy was employed.³⁸ The FTIR spectra of composite hydrogel samples before and after the adsorption of Cu^{2+} are illustrated in Figure 2. As can be noticed, some changes in the spectra are visible before and after the adsorption. The broad band at 3300 to 3500 cm^{-1} was attributed to the ($-\text{OH}$) stretching vibration, and the significant characteristic band within the range of 1500 to 1650 cm^{-1} indicates $-\text{OH}$ bending in all samples. The peaks at 1660 and 1573 cm^{-1} presented in Figure 2a shifted to 1652 and 1565 cm^{-1} in Figure 2b, and the

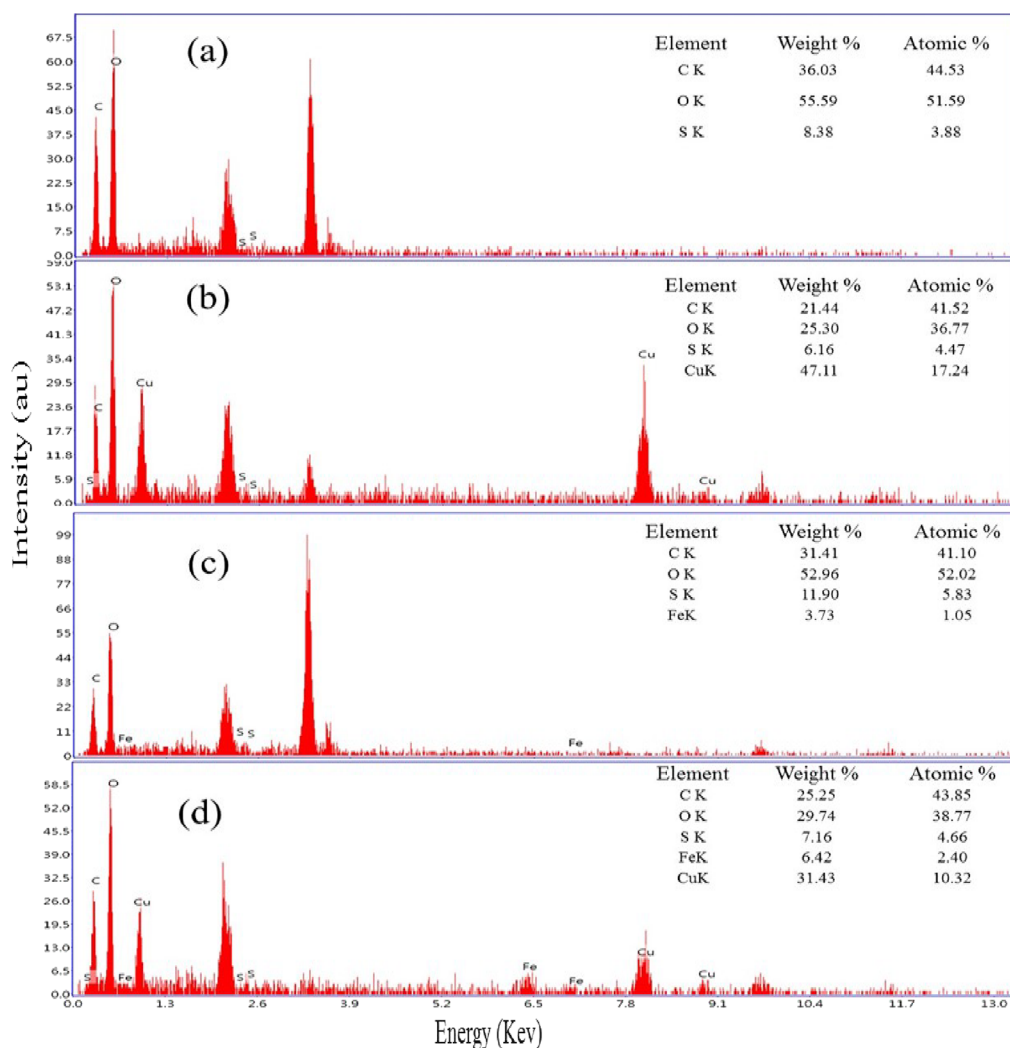


Figure 4. EDX elemental analysis: (a) St-g-PAA/CNFs before adsorption, (b) St-g-PAA/CNFs after adsorption, (c) M-St-g-PAA/CNFs before adsorption, and (d) M-St-g-PAA/CNFs after adsorption.

peaks at 1716 and 1580 cm^{-1} (Figure 2c) shifted to 1710 and 1562 cm^{-1} (Figure 2d), respectively.³¹ The observed shifts and changes suggest a metal-surrounding process via ion exchange and chelation that coexist between carboxyl groups (COOH) and carboxylate (COO^-) and Cu^{2+} ions on the surface of the samples. The incorporation of CNFs within the matrix resulted in extra peaks at 1056 cm^{-1} in Figure 2a, 1037 cm^{-1} in Figure 2b, 1045 cm^{-1} in Figure 2c, and 1039 cm^{-1} in Figure 2d, which are attributable to the asymmetrical vibrations of C–O–C and stretching vibrations of C–C and C–O asymmetric pyran rings.³¹ The band at 422 cm^{-1} that appeared in the FTIR spectrum of Fe_3O_4 is related to the vibration of Fe–O. However, the Fe–O characteristic peak in the magnetic hydrogel after adsorption of Cu^{2+} was shifted to a lower wavenumber, which may be a result of the adsorption of Cu^{2+} on the nanoparticle surface and the physical effect.³⁹

3.2. Morphology of the Adsorbent. The morphological changes of hydrogel before and after the adsorption of Cu^{2+} were investigated by SEM analysis. As presented, samples in Figure 3a,b for St-g-PAA/CNFs and M-St-g-PAA/CNFs show an irregular porous structure before adsorption. These pores connect together and form a network structure. This network-like structure provides functional channels for water molecules and other ions to facilitate them in and out of hydrogel.⁴⁰ It is

clear that Cu^{2+} ion adsorption has significantly changed the morphology of hydrogels' voids. It is worth mentioning that hydrogels became rougher and more brittle after the adsorption of Cu^{2+} ions.

To confirm the incorporation of Fe_3O_4 NPs into the magnetic hydrogel matrix and the results of the removal of Cu^{2+} , EDX analysis was conducted on hydrogels. As can be observed from Figure 4c, it was clearly indicated that some of the nanoparticles were present over the surface of the M-St-g-PAA/CNFs hydrogel matrix (about 2%). Also, the presence of Cu^{2+} ions was confirmed in the two matrices of hydrogel biosorbents after adsorption (Figure 4b,d). Dil and Sadeghi found similar results for the adsorption of Cu^{2+} on the surface of the nanosilver/gelatin-poly(acrylic acid) hydrogel.³⁶

3.3. Magnetic Properties. The photographs of the powder form of hydrogel and magnetic hydrogel are shown in Figure 5a,b. Figure 5c,d indicates that the magnetic hydrogel adsorbent was able to reclaim by the external magnetic field. This property of the hydrogel adsorbent is virtually significant for its convenient recovery and reusability. The magnetic behaviors of the Fe_3O_4 nanoparticle and magnetic hydrogel were analyzed by vibrating sample magnetometry (VSM) at room temperature. Figure 5e presents the plot of magnetization versus the applied magnetic field strength of M-St-g-PAA/CNFs and pristine

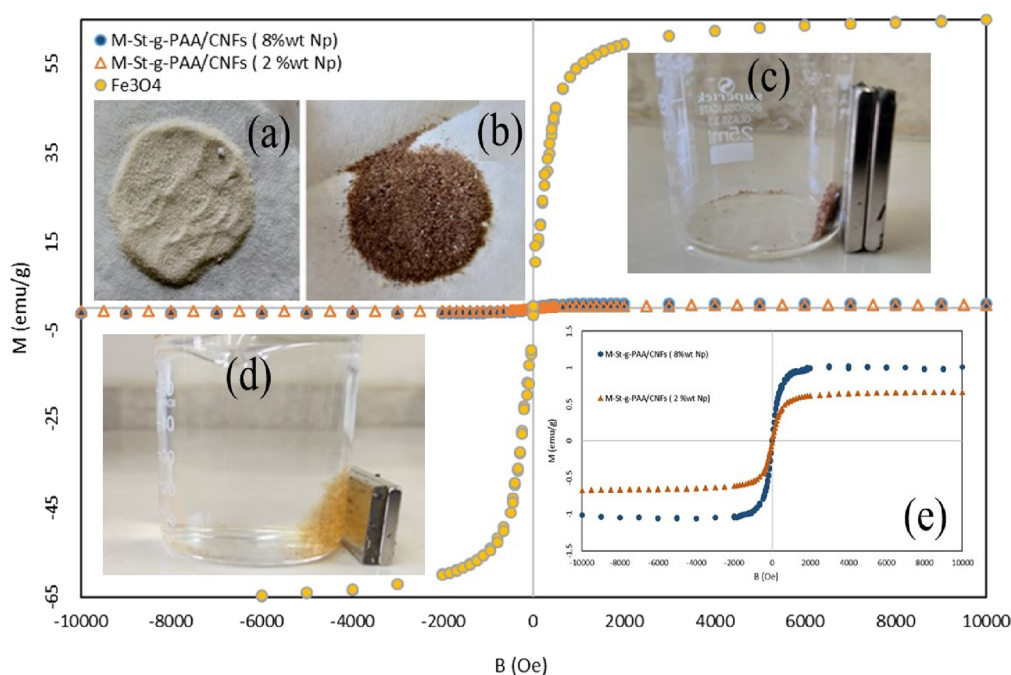


Figure 5. Photographs of the powder form of (a) St-g-PAA/CNFs and (b) M-St-g-PAA/CNFs, (c) separated magnetic hydrogel by the permanent magnet in dry form and (d) in swelling form in water, and (e) plot of magnetization (M) as a function of applied magnetic field (B) for Fe_3O_4 nanoparticles and the magnetic hydrogel nanocomposite M-St-g-PAA/CNFs at room temperature.

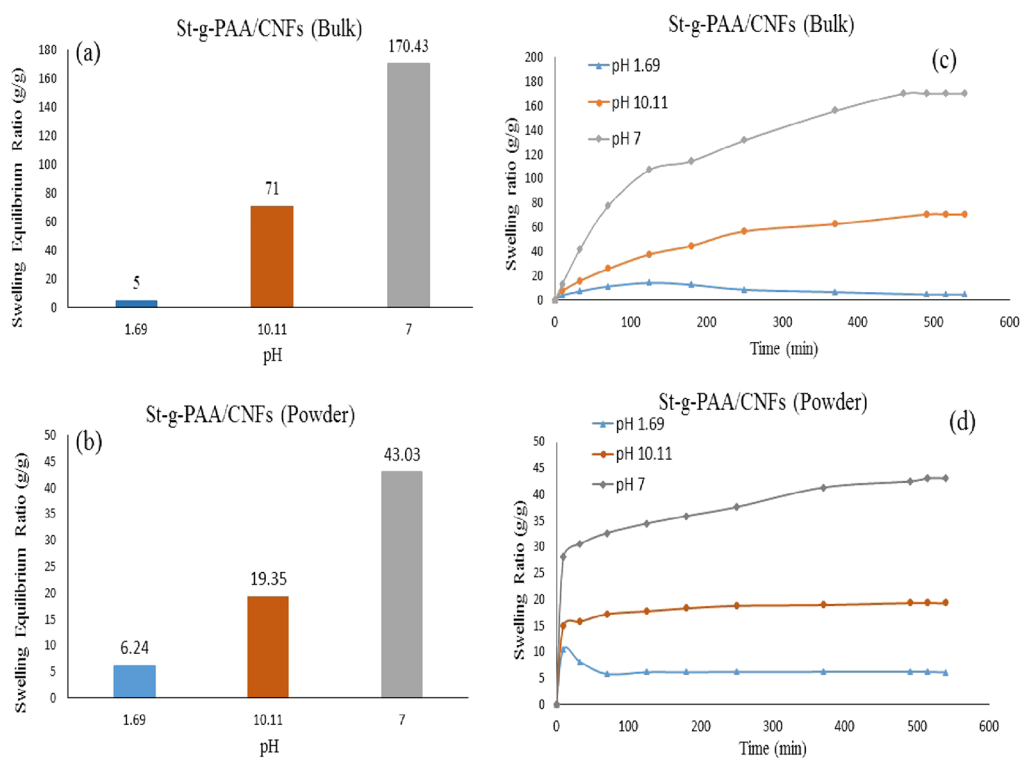


Figure 6. (a) Influence of pH on the equilibrium swelling ratio of the St-g-PAA/CNFs hydrogel as a bulk and (b) as a powder. (c) Swelling ratio of the St-g-PAA/CNFs hydrogel as a bulk in different pH solutions and (d) as a powder.

Fe_3O_4 nanoparticles. The results demonstrate that Fe_3O_4 nanoparticles and magnetic hydrogel exhibited superparamagnetic and paramagnetic behaviors, respectively. Although the magnetization ability of both was confirmed when exposed to a magnetic field, however, no permanent magnetization existed after the magnetic field removal, which plays a crucial role in

many important applications such as drug delivery, magnetic resonance imaging, magnetic separation, etc.^{30,41,42} The pristine Fe_3O_4 nanoparticles exhibit induced magnetization of 60–65 emu/g at the plateau (at $B \sim 2\text{--}10$ kOe), which is in agreement with the reported results in the literature.^{28,43} At the plateau, in an applied magnetic field of $\sim 2\text{--}10$ kOe range for M-St-g-PAA/

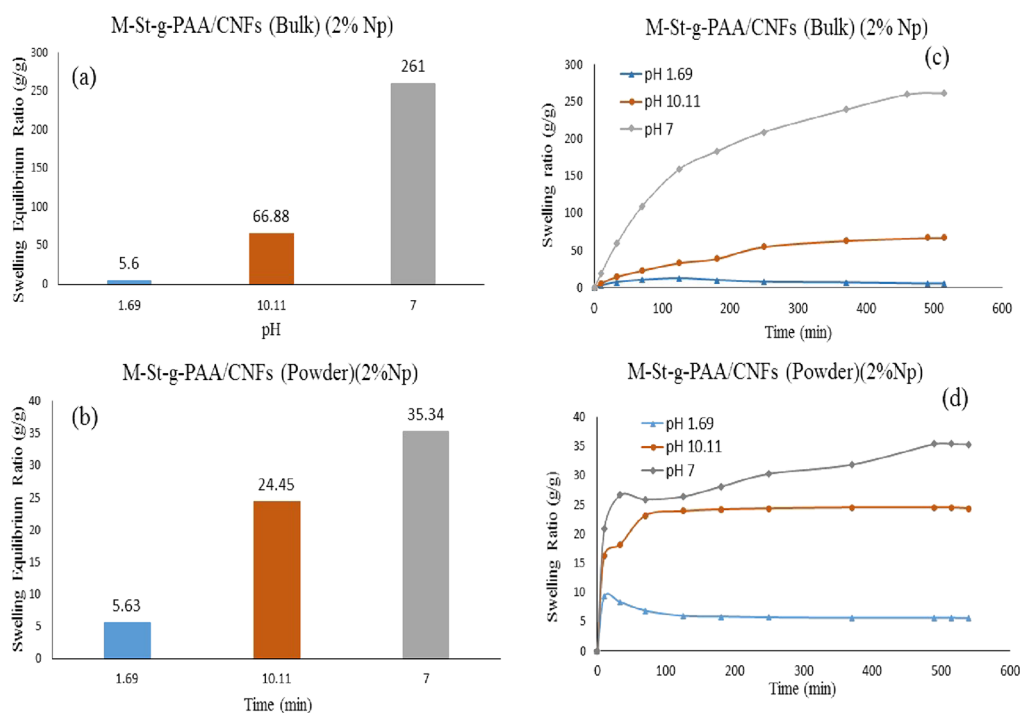


Figure 7. (a) Influence of pH during swelling on the equilibrium swelling ratio of the M-St-g-PAA/CNFs hydrogel as a bulk and (b) as a powder. (c) Swelling ratio of the M-St-g-PAA/CNFs hydrogel as a bulk in different pH solutions and (d) as a powder.

CNFs with 2 and 8 wt % NPs, the induced magnetization values in the paramagnetic hydrogel were found to be about 0.6–0.66 and 1–1.04 emu/g, respectively. The results indicate a reduction in saturation magnetization of M-St-g-PAA/CNFs compared to that of pristine Fe_3O_4 , mainly due to the low content of embedded and dispersed Fe_3O_4 nanoparticles (2 and 8 wt %) in the hydrogel matrix. Similar results have been reported previously.¹²

3.4. Swelling Measurement. Hydrogels sensitive to pH are generated by adding an acidic or basic functional group to the polymer structure; these functional groups either accept or release protons in response to the changes in pH value and are mostly responsible for determining the swelling behavior of the hydrogel for a given solution.²⁸ The hydrogels St-g-PAA/CNFs and M-S-g-PAA/CNFs exhibited remarkable pH sensitivity (the pH of the solutions was adjusted by adding HCl and NaOH (1 mol·L⁻¹)). The pH-sensitive swelling properties of the hydrogels were investigated, and they are shown in Figures 6 and 7. The swelling rate (SR) of the hydrogel samples was determined using the gravimetric method. Figures 6 and 7 show the swelling behavior in terms of the swelling equilibrium and swelling ratio of the four types of hydrogels, including bulk and powder forms with and without magnetic particles. As can be noticed, both swelling equilibrium and ratio were decreased by decreasing the pH value from neutral (pH = 7) to acidic (pH = 1.69) and increasing the pH value from neutral (pH = 7) to basic (pH = 10.11). The results show that the change in pH values from pH 1.69 to pH 7 causes a significant variation in the equilibrium swelling ratio.

As can be observed in Figures 6 and 7, the final swelling equilibrium ratio in bulk hydrogel is higher than that in powder hydrogel. The reason is that the hydrogel swelling is mainly due to diffusion and capillary rise of water into a hydrogel.⁴⁴ In bulk hydrogel, the three-dimensional structure of the hydrogel creates more capillary space to hold water molecules, while

when the hydrogel turns into a powder form, the three-dimensional structures are fractured, and there is less space to hold water.

Table 1 shows the swelling rate (SR) and equilibrium swelling (S_e) of St-g-PAA/CNFs and M-St-g-PAA/CNFs at different pH values for two states of bulk and powder.

Table 1. Swelling Characteristics of the St-g-PAA/CNFs and M-St-g-PAA/CNFs Hydrogels at Different pH Values

pH	swelling rate (SR) (g/(g·min))			
	St-g-PAA/CNFs		M-St-g-PAA/CNFs	
	bulk	powder	bulk	powder
1.69	0.26	not fitted	0.24	not fitted
7	1	4.46	1.28	2.78
10.11	0.32	2.32	0.29	1.68

The results reveal that there is a strong enhancement in the swelling behavior (in terms of SR and S_e) of two hydrogels when the pH value is 7. The variation in swelling behavior can be attributed to the fact that as the pH value increases, the ionization of available $-\text{COOH}$ and $-\text{OH}$ functional groups in the hydrogel enhances gradually, which causes a high electrostatic repulsion between neighboring ionized COO^- groups of the network structure, and the concentration of ions inside the hydrogel increases than in the surrounding solution, which causes an osmotic pressure difference between the hydrogel and the solution and results in a water flow into the hydrogel and, consequently, a swelling in the hydrogel.²⁸ However, at pH > 7, the high concentration of OH^- will result in extra crosslinking in the hydrogel.^{45,46}

3.5. Adsorption of Cu^{2+} onto Bulk and Powder Forms of Hydrogels. The effects of bulk and powder forms of St-g-PAA/CNFs and M-St-g-PAA/CNFs hydrogels on Cu^{2+} adsorption were investigated. The results are presented in

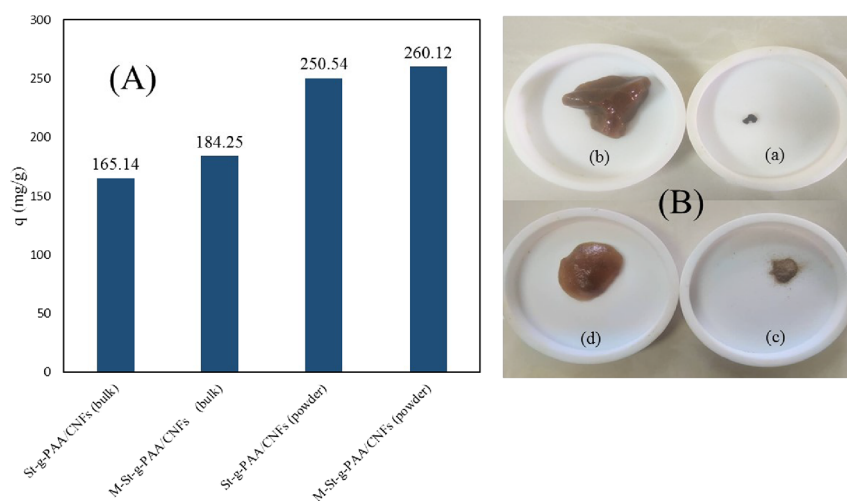


Figure 8. (A) Comparison of the Cu^{2+} adsorbent onto bulk and powder hydrogels (initial Cu^{2+} concentration of 600 mg/L and pH = 5) and (B) photographs showing the swelling bulk and powder hydrogels of M-St-g-PAA/CNFs. (a, c) Before swelling and (b, d) after swelling.

Figure 8. As shown, the adsorption capacity of powder hydrogels is higher than that of bulk form due to the increase in available surface area and, consequently, higher active sites of the adsorbent.^{47,48} According to Table 1, the slow kinetics of bulk hydrogel makes it cost-ineffective for application on a large scale. It has been reported that slow kinetics is attributed to long diffusion paths of the contaminant molecules in reaching their adsorption sites within the hydrogel.⁴⁹ Therefore, it is expected that the hydrogel with a much smaller particle size would solve the problem of the slow kinetics of pollutant removal.

In the economic point of view, less amount of hydrogel would be consumed for the powder hydrogel to achieve the same amount of copper removal compared to that of the bulk hydrogel. For this reason, the powder form of hydrogels was used for the rest of the study.

Figure 8B shows the magnetic hydrogel in bulk and powder forms before and after water absorption.

3.6. Effect of pH. To find the optimum adsorption condition, the effect of pH on the adsorption capacity for Cu^{2+} on M-St-g-PAA/CNFs was investigated. The variation of Cu^{2+} adsorption capacity with a change in pH from 2 to 7 by using HCl and NaOH solution (1 M) is illustrated in Figure 9. The adsorption capacity for Cu^{2+} increased gradually with increasing pH until the value of 5. The reason was that strong complexation interactions of Cu^{2+} via numerous $-\text{COO}^-$

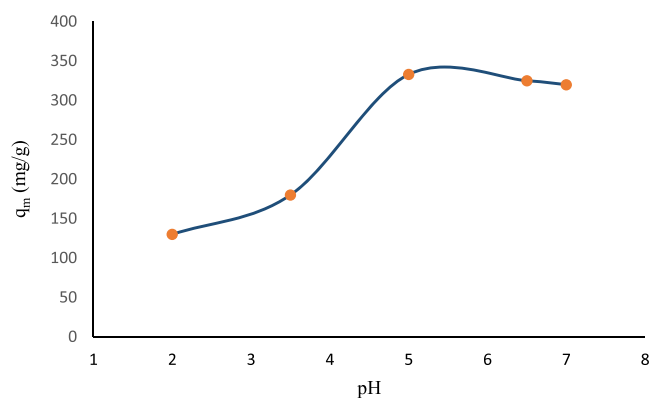


Figure 9. Effect of pH on Cu^{2+} removal by M-St-g-PAA/CNFs (initial Cu^{2+} concentration of 600 mg/L).

groups onto the hydrogel skeleton caused relatively high adsorption capacity. The low adsorption capacity in the low-pH region was attributed to the fact that the dissociation of all the carboxyl groups was restrained and to the competitive adsorption between H^+ and Cu^{2+} . At pH higher than 5, Cu^{2+} starts to precipitate by (OH^-) ions, and the adsorption of Cu^{2+} is invalid. Therefore, the removal of Cu^{2+} was tested at a pH below 7 to prevent sedimentation of metal ions and ensure the homogeneity of the solution. According to Figure 9, it can be seen that the maximum capacity of adsorption of Cu^{2+} occurred at a pH of about 5. Thus, during the experiments, the initial pH value of the Cu^{2+} solution is set to 5.

3.7. Adsorption Isotherms. Adsorption isotherms describe the interaction of the adsorbent and adsorbed surfaces. Therefore, they are always considered as an essential factor for determining the adsorbent capacity and optimizing the adsorbent consumption.²⁰ In this study, the adsorption data of St-g-PAA/CNFs and M-St-g-PAA/CNFs powder hydrogels for Cu^{2+} were investigated with the Langmuir, Freundlich, and Temkin models, which are common adsorption isotherm models (Section 2.6). The linear isotherm parameters are presented in Table 2. According to the results, the Langmuir

Table 2. Comparison of Linear Isotherm Parameters for Cu^{2+} Adsorptions on Two Adsorbents

isotherm model	adsorbent		
	St-g-PAA/CNFs	M-St-g-PAA/CNFs (2% NPs)	M-St-g-PAA/CNFs (8% NPs)
Langmuir model			
q_{max} (mg/g)	322.58	333.33	555.55
K_L (L/mg)	0.046	0.054	0.013
R^2	0.94	0.90	0.99
Freundlich model			
K_F (mg/g)(mg/L) ^{1/n}	108.90	83.02	10.37
N	5.63	4.29	1.77
R^2	0.855	0.7985	0.94
Temkin model			
b_T (J/mol)	60.79	45.7	21.27
A_T (L/g)	5.51	1.15	8.33
R^2	0.82	0.734	0.9

model for both adsorbents indicated the highest R^2 values compared with the two others. Thus, the adsorption process has happened monolithically followed by the Langmuir model. The calculated amount of monolayer adsorption capacity and the constant value of the Langmuir isotherm (which implies the binding between the adsorbate and the adsorbent) in Table 2 indicate the higher adsorption capacity and the binding tendency for the magnetic hydrogels compared to the hydrogel without magnetic nanoparticles (Fe_3O_4). It could be due to the presence of Fe–O functional groups in their structure that interact with metal ions and high surface area in a magnetic hydrogel, which will cause higher adsorption capacity consequently.

3.8. Adsorption Kinetics. The rate of adsorption to time is investigated by the kinetic test with the explanation of the adsorption mechanism by the adsorbent. Four mathematical models of adsorption kinetics, including pseudo-first-order (PS-I), pseudo-second-order (PS-II), Elovich, and intra-particle diffusion models (Section 2.7), were used to investigate the adsorption rate of Cu^{2+} ions for bio-adsorbents. The kinetic parameters obtained for adsorption kinetic models are presented in Table 3.

Table 3. Comparison of Kinetic Parameters for Cu^{2+} Ion Adsorptions on Powder Hydrogel Adsorbents

kinetic model	adsorbent		
	St-g-PAA/ CNFs	M-St-g-PAA/CNFs (2% NPs)	M-St-g-PAA/CNFs (8% NPs)
pseudo-first-order model			
q_e (mg/g)	256.73	257.24	267.73
k_1 (1/min)	0.003	0.004	0.0039
R^2	0.781	0.812	0.96
pseudo-second-order model			
q_e (mg/g)	232.56	228.5	333.33
k_2 (g/mg·min)	0.0016	0.0026	0.0013
R^2	0.96	0.95	0.999
Elovich model			
α (mg/g/min)	120.07	48.34	90.11
β (g/mg)	0.0244	0.02	0.013
R^2	0.431	0.611	0.69
intra-particle diffusion model			
k_i (mg/g/min ^{0.5})	16.66	18.27	20.031
I (mg/g)	59.43	57.80	130.52
R^2	0.84	0.79	0.53

In Table 3, the results confirmed that Cu^{2+} adsorptions of St-g-PAA/CNFs and M-St-g-PAA/CNFs correspond to PS-II with higher correlation coefficients than the other models. Similar results were reported in previous studies.⁵ Therefore, their surfaces involved chemisorption,⁵⁰ and their adsorption mechanism was the physiochemical interaction between the adsorbate (Cu^{2+}) and the adsorbent (St-g-PAA/CNFs and M-St-g-PAA/CNFs). According to the obtained results, magnetizing the hydrogel aimed at its application and facilitating the separation of the adsorbent from the solution after the adsorption process have even increased the adsorption capacity of the adsorbent, and it can be the advantage of the magnetic hydrogels.

Figure 10 shows the mechanism of Cu^{2+} ion adsorption by the M-St-g-PAA/CNFs hydrogel schematically.

The surface of the M-St-g-PAA/CNFs hydrogel has a significant number of carboxyl groups ($-\text{COOH}$) on the main structure of the hydrogel. It is expected that the adsorption process occurs through the ion exchange and chelation between Cu^{2+} ions and the ionized and deionized carboxyl groups inside the hydrogel. In addition, the presence of CNFs in the hydrogel matrix with high surface area and ample hydroxyl groups ($-\text{OH}$) in its backbone cellulosic structure increases the interactions with metal ions and, consequently, causes higher adsorption capacity. In addition, the presence of Fe_3O_4 magnetic nanoparticles with high surface area can help in the adsorption of Cu^{2+} . This is because at pH values higher than the pH of the isoelectric point of Fe_3O_4 nanoparticles (pHpzc occurs at a pH of 3–4),⁵¹ the OH^- concentration increases and the protonated effect of the surface of magnetic nanoparticles weakens and results in the content of $-\text{FeO}^-$ increasing, which is helpful to the adsorption of Cu^{2+} .⁵¹ Figure 9 shows that the maximum capacity of adsorption of Cu^{2+} occurred at a pH of about 5, and the experiments in this work were carried out at pH = 5 (see Section 3.6).

As summarized in Table 4, the comparative results demonstrate that the prepared magnetic hydrogel adsorbent in this study has a higher adsorption capacity of Cu^{2+} than other hydrogel adsorbents reported previously. The synthesized magnetic hydrogel reinforced by CNFs in this work has different functional groups in the main structure of the hydrogel and different active centers on the cellulose nanofibers and also magnetic nanoparticles. Functional groups are of prime importance in the absorption process. On the other hand, the presence of Fe_3O_4 magnetic nanoparticles with high surface area can help in the adsorption of Cu^{2+} . These cause higher performance as compared to previous works. Therefore, the hydrogel synthesized in this work has adequate adsorption capacity and can compete with other acceptable adsorbents.

3.9. Desorption and Reusability. Because the hydrogel containing 8% of nanoparticles showed the highest amount of adsorption, the recovery process was performed by this hydrogel with 0.1 M hydrochloric acid solution. Figure 11 shows the adsorption efficiency of the adsorbents for four cycles of the adsorption–desorption procedure. The adsorption efficiency decreased slightly after each cycle. The average adsorption and desorption efficiencies after four cycles are 81.43 and 83.35%, respectively. The results suggested good performance for the regeneration of the magnetic hydrogel.

4. CONCLUSIONS

In this work, the swelling and adsorption behaviors of two types of hydrogels (St-g-PAA/CNFs and M-St-g-PAA/CNFs) in bulk and powder forms were compared. A fast rate of swelling and higher adsorption capacity were seen in powder magnetic hydrogels. It was demonstrated that the variation in the equilibrium swelling ratio of two hydrogels is reportedly high in response to the change in pH. According to FTIR, SEM, EDX, and VSM technique results, the Fe_3O_4 nanoparticles were well synthesized and stabilized in the structure of hydrogel. Two types of hydrogels were synthesized in powder form to remove Cu^{2+} ions. The results showed that the creation of magnetic properties in the hydrogel, in addition to the ease of separation by a magnetic field, assists in increasing the adsorption of the hydrogel. Fitting in the experimental data with the isotherm and kinetic models showed that the data had the best correlation

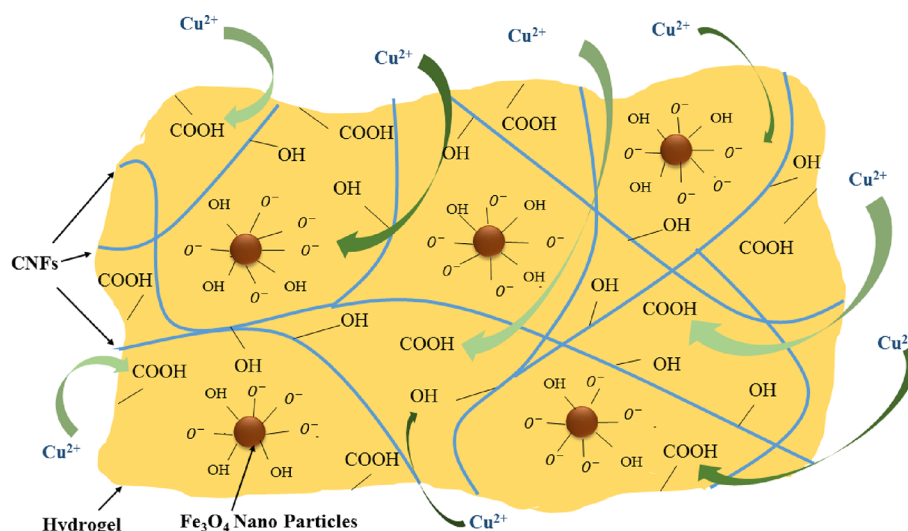


Figure 10. Mechanism of Cu^{2+} ion adsorption.

Table 4. Comparison of Adsorption of Cu^{2+} on the Different Hydrogels

hydrogel	q_m (mg/g)	reference
CMS-g-PVI/PVA/ Fe_3O_4	83.6	52
(P(AMPS-co-VDT)	175.75	53
poly(acrylic acid)/penytriethoxytrisilane (PTES)	143.4	54
lignin-based hydrogel	290	55
poly(acrylic acid/chestnut shell pigment) hydrogel	200.3	56
P(AA-MMA)/MGO/CA-CD/ NH_2	140.50	30
GO/PA-AMPS/SA	230.8	57
modified kaolin	106.4	58
M-St-g-PAA/CNFs (2 wt % NPs)	333.33	this work
M-St-g-PAA/CNFs (8 wt % NPs)	555.56	this work

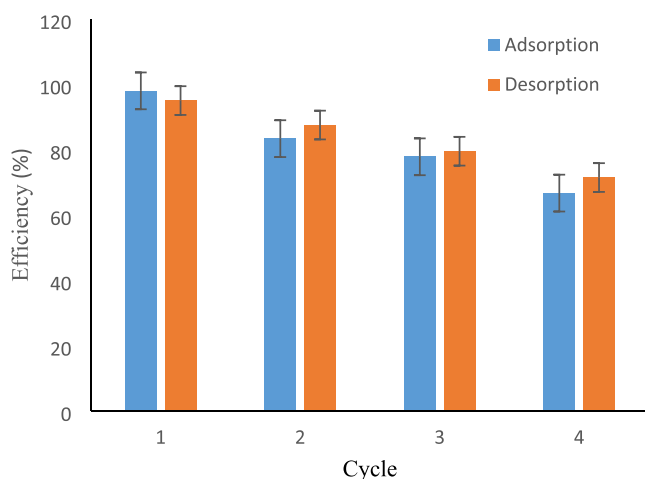


Figure 11. Four cycles of copper ion adsorption/desorption of M-St-g-PAA/CNFs.

with Langmuir and pseudo-second-order models individually. Compared with other hydrogels and examined reusability, the synthesized hydrogel has a satisfactory performance due to the amount of ion removal. This magnetic hydrogel will be a suitable candidate for use in the continuous process of heavy metal ion removal.

AUTHOR INFORMATION

Corresponding Author

Nasrin Etesami – Department of Chemical Engineering, Isfahan University of Technology, Isfahan 84156-83111, Iran;
orcid.org/0000-0002-4370-1566; Email: netesami@iut.ac.ir

Authors

Nasime Mirhoseini Renani – Department of Chemical Engineering, Isfahan University of Technology, Isfahan 84156-83111, Iran

Tayebeh Behzad – Department of Chemical Engineering, Isfahan University of Technology, Isfahan 84156-83111, Iran

Complete contact information is available at:

<https://pubs.acs.org/10.1021/acsomega.3c01655>

Notes

The authors declare no competing financial interest.

ACKNOWLEDGMENTS

Partial financial support of the Isfahan University of Technology is gratefully appreciated.

REFERENCES

- (1) Verma, M. L.; Thakur, M.; Randhawa, J. S.; Sharma, D.; Thakur, A.; Meehnan, H.; Jana, A. K., Biotechnological Applications of Fungal Enzymes with Special Reference to Bioremediation. In *Environmental Biotechnology Vol. 2*; Gothandam, K. M.; Ranjan, S.; Dasgupta, N.; Lichtfouse, E., Eds. Springer International Publishing: Cham, 2020; pp. 221–247.
- (2) Verma, M. L.; Kumar, S.; Das, A.; Randhawa, J. S.; Chamundeeswari, M. Chitin and chitosan-based support materials for enzyme immobilization and biotechnological applications. *Environ. Chem. Lett.* **2020**, *18*, 315–323.
- (3) Reynolds, T. D.; Richards, P. A., *Unit Operations and Processes in Environmental Engineering*; PWS Publishing Company: 1996.
- (4) Demirbilek, C.; Dinç, C. Ö. Synthesis of diethylaminoethyl dextran hydrogel and its heavy metal ion adsorption characteristics. *Carbohydr. Polym.* **2012**, *90*, 1159–1167.
- (5) Hua, R.; Li, Z. Sulfhydryl functionalized hydrogel with magnetism: Synthesis, characterization, and adsorption behavior study for heavy metal removal. *Chem. Eng. J.* **2014**, *249*, 189–200.

- (6) Liu, C.; Bai, R. Recent advances in chitosan and its derivatives as adsorbents for removal of pollutants from water and wastewater. *Curr. Opin. Chem. Eng.* **2014**, *4*, 62–70.
- (7) Jain, M.; Garg, V.; Garg, U.; Kadirvelu, K.; Sillanpää, M. Cadmium Removal from Wastewater using Carbonaceous Adsorbents Prepared from Sunflower Waste. *Int. J. Environ. Res.* **2015**, *9*, 1079–1088.
- (8) Rosales, E.; Mejjide, J.; Pazos, M.; Sanromán, M. A. Challenges and recent advances in biochar as low-cost biosorbent: From batch assays to continuous-flow systems. *Bioresour. Technol.* **2017**, *246*, 176–192.
- (9) Hegde, V.; Uthappa, U. T.; Suneetha, M.; Altalhi, T.; Soo Han, S.; Kurkuri, M. D. Functional porous Ce-UiO-66 MOF@Keratin composites for the efficient adsorption of trypan blue dye from wastewater: A step towards practical implementations. *Chem. Eng. J.* **2023**, *461*, No. 142103.
- (10) Bhat, S.; Uthappa, U. T.; Sadhasivam, T.; Altalhi, T.; Soo Han, S.; Kurkuri, M. D. Abundant cilantro derived high surface area activated carbon (AC) for superior adsorption performances of cationic/anionic dyes and supercapacitor application. *Chem. Eng. J.* **2023**, *459*, No. 141577.
- (11) Häring, M.; Schiller, J.; Mayr, J.; Grijalvo, S.; Eritja, R.; Díaz, D. Magnetic Gel Composites for Hyperthermia Cancer Therapy. *Gels* **2015**, *1*, 135–161.
- (12) Souda, P.; Sreejith, L. Magnetic hydrogel for better adsorption of heavy metals from aqueous solutions. *J. Environ. Chem. Eng.* **2015**, *3*, 1882–1891.
- (13) Mirabedini, M.; Kassae, M. Z.; Poorsadeghi, S. Novel Magnetic Chitosan Hydrogel Film, Crosslinked with Glyoxal as an Efficient Adsorbent for Removal of Toxic Cr(VI) from Water. *Arabian J. Sci. Eng.* **2017**, *42*, 115–124.
- (14) Pu, S.; Ma, H.; Zinchenko, A.; Chu, W. Novel highly porous magnetic hydrogel beads composed of chitosan and sodium citrate: an effective adsorbent for the removal of heavy metals from aqueous solutions. *Environ. Sci. Pollut. Res.* **2017**, *24*, 16520–16530.
- (15) Wang, Y.; Li, B.; Xu, F.; Han, Z.; Wei, D.; Jia, D.; Zhou, Y. Tough Magnetic Chitosan Hydrogel Nanocomposites for Remotely Stimulated Drug Release. *Biomacromolecules* **2018**, *19*, 3351–3360.
- (16) Lin, F.; Zheng, J.; Guo, W.; Zhu, Z.; Wang, Z.; Dong, B.; Lin, C.; Huang, B.; Lu, B. Smart cellulose-derived magnetic hydrogel with rapid swelling and deswelling properties for remotely controlled drug release. *Cellulose* **2019**, *26*, 6861–6877.
- (17) Qie, Z.; Wang, L.; Sun, F.; Xiang, H.; Wang, H.; Gao, J.; Zhao, G.; Fan, X. Tuning porosity of coal-derived activated carbons for CO₂ adsorption. *Front. Chem. Sci. Eng.* **2022**, *16*, 1345–1354.
- (18) Amiralian, N.; Mustapic, M.; Hossain, M. S. A.; Wang, C.; Konarova, M.; Tang, J.; Na, J.; Khan, A.; Rowan, A. Magnetic nanocellulose: A potential material for removal of dye from water. *J. Hazard. Mater.* **2020**, *394*, No. 122571.
- (19) Lu, Q.; Zhang, Y.; Hu, H.; Wang, W.; Huang, Z.; Chen, D.; Yang, M.; Liang, J. In Situ Synthesis of a Stable Fe₃O₄@Cellulose Nanocomposite for Efficient Catalytic Degradation of Methylene Blue. *Nanomaterials* **2019**, *9*, 275.
- (20) Jamali, M.; Akbari, A. Facile fabrication of magnetic chitosan hydrogel beads and modified by interfacial polymerization method and study of adsorption of cationic/anionic dyes from aqueous solution. *J. Environ. Chem. Eng.* **2021**, *9*, No. 105175.
- (21) Liu, W.; Liu, X.; Chang, J.; Jiang, F.; Pang, S.; Gao, H.; Liao, Y.; Yu, S. Efficient removal of Cr(VI) and Pb(II) from aqueous solution by magnetic nitrogen-doped carbon. *Front. Chem. Sci. Eng.* **2021**, *15*, 1185–1196.
- (22) Konwar, A.; Gogoi, A.; Chowdhury, D. Magnetic alginate–Fe₃O₄ hydrogel fiber capable of ciprofloxacin hydrochloride adsorption/separation in aqueous solution. *RSC Adv.* **2015**, *5*, 81573–81582.
- (23) Su, R.; Wang, F.; Ding, J.; Li, Q.; Zhou, W.; Liu, Y.; Gao, B.; Yue, Q. Magnetic hydrogel derived from wheat straw cellulose/feather protein in ionic liquids as copper nanoparticles carrier for catalytic reduction. *Carbohydr. Polym.* **2019**, *220*, 202–210.
- (24) Zhao, W.; Odelius, K.; Edlund, U.; Zhao, C.; Albertsson, A.-C. In Situ Synthesis of Magnetic Field-Responsive Hemicellulose Hydrogels for Drug Delivery. *Biomacromolecules* **2015**, *16*, 2522–2528.
- (25) Chen, Z.; Wang, Y.-F.; Zeng, J.; Zhang, Y.; Zhang, Z.-B.; Zhang, Z.-J.; Ma, S.; Tang, C.-M.; Xu, J.-Q. Chitosan/polyethyleneimine magnetic hydrogels for adsorption of heavy metal ions. *Iran. Polym. J.* **2022**, *31*, 1273–1282.
- (26) Cruz, H.; Yap Gabon, M.; Salehin, S.; Seviour, T.; Laycock, B.; Pikaar, I. Magnetic poly(acrylic acid)-based hydrogels for rapid ammonium sorption and efficient sorbent separation from sewage. *Environ. Sci. Ecotechnology* **2021**, *6*, No. 100097.
- (27) Zhou, Y.; Fu, S.; Zhang, L.; Zhan, H.; Levit, M. V. Use of carboxylated cellulose nanofibrils-filled magnetic chitosan hydrogel beads as adsorbents for Pb(II). *Carbohydr. Polym.* **2014**, *101*, 75–82.
- (28) Singh, R.; Pal, D.; Chattopadhyay, S. Target-Specific Superparamagnetic Hydrogel with Excellent pH Sensitivity and Reversibility: A Promising Platform for Biomedical Applications. *ACS Omega* **2020**, *5*, 21768–21780.
- (29) Jafari, H.; Atlasi, Z.; Mahdavinia, G. R.; Hadifar, S.; Sabzi, M. Magnetic κ -carrageenan/chitosan/montmorillonite nanocomposite hydrogels with controlled sunitinib release. *Mater. Sci. Eng., C* **2021**, *124*, No. 112042.
- (30) Yan, J.; Li, K. A magnetically recyclable polyampholyte hydrogel adsorbent functionalized with β -cyclodextrin and graphene oxide for cationic/anionic dyes and heavy metal ion wastewater remediation. *Sep. Purif. Technol.* **2021**, *277*, No. 119469.
- (31) Bahadoran Baghbadorani, N.; Behzad, T.; Etesami, N.; Heidarian, P. Removal of Cu²⁺ ions by cellulose nanofibers-assisted starch-g-poly(acrylic acid) superadsorbent hydrogels. *Composites, Part B* **2019**, *176*, No. 107084.
- (32) Guspita, D.; Ulianas, A. Optimization of complex NH₃ with Cu²⁺ ions to determine levels of ammonia by UV-Vis spectrophotometer. *J. Phys.: Conf. Ser.* **2020**, *1481*, No. 012040.
- (33) Threpanich, A.; Praipipat, P. Powdered and beaded lemon peels-doped iron (III) oxide-hydroxide materials for lead removal applications: Synthesis, characterizations, and lead adsorption studies. *J. Environ. Chem. Eng.* **2021**, *9*, No. 106007.
- (34) Zhang, M.-K.; Zhang, X.-H.; Han, G.-Z. Magnetic alginate/PVA hydrogel microspheres with selective adsorption performance for aromatic compounds. *Sep. Purif. Technol.* **2021**, *278*, No. 119547.
- (35) Hekmatzadeh, A. A.; Karimi-Jashni, A.; Talebbeydokhti, N.; Kløve, B. Adsorption kinetics of nitrate ions on ion exchange resin. *Desalination* **2013**, *326*, 125–134.
- (36) Dil, N. N.; Sadeghi, M. Free radical synthesis of nanosilver/gelatin-poly (acrylic acid) nanocomposite hydrogels employed for antibacterial activity and removal of Cu(II) metal ions. *J. Hazard. Mater.* **2018**, *351*, 38–53.
- (37) Heidarzadeh-Samani, M.; Behzad, T.; Mehrabani-Zeinabad, A. Development of a continuous fixed-bed column to eliminate cadmium(II) ions by starch-g-poly(acrylic acid)/cellulose nanofiber bio-nanocomposite hydrogel. *Environ. Sci. Pollut. Res.* **2021**, *28*, 57902–57917.
- (38) Zhang, Y.; Gao, P.; Zhao, L.; Chen, Y. Preparation and swelling properties of a starch-g-poly(acrylic acid)/organo-mordenite hydrogel composite. *Front. Chem. Sci. Eng.* **2016**, *10*, 147–161.
- (39) Sun, X. F.; Liu, B.; Jing, Z.; Wang, H. Preparation and adsorption property of xylan/poly(acrylic acid) magnetic nanocomposite hydrogel adsorbent. *Carbohydr. Polym.* **2015**, *118*, 16–23.
- (40) Kurdtabar, M.; Rezanejad Bardajee, G. Drug release and swelling behavior of magnetic iron oxide nanocomposite hydrogels based on poly(acrylic acid) grafted onto sodium alginate. *Polym. Bull.* **2020**, *77*, 3001–3015.
- (41) Wang, Y.; Zhang, X.-Y.; Luo, Y.-L.; Xu, F.; Chen, Y.-S.; Su, Y.-Y. Dual stimuli-responsive Fe₃O₄ graft poly(acrylic acid)-block-poly(2-methacryloyloxyethyl ferrocenecarboxylate) copolymer micromicelles: surface RAFT synthesis, self-assembly and drug release applications. *J. Nanobiotechnol.* **2017**, *15*, 76.
- (42) Guo, W.; Hu, W.; Pan, J.; Zhou, H.; Guan, W.; Wang, X.; Dai, J.; Xu, L. Selective adsorption and separation of BPA from aqueous

solution using novel molecularly imprinted polymers based on kaolinite/Fe₃O₄ composites. *Chem. Eng. J.* **2011**, *171*, 603–611.

(43) Huang, Y.; Liu, M.; Chen, J.; Gao, C.; Gong, Q. A novel magnetic triple-responsive composite semi-IPN hydrogels for targeted and controlled drug delivery. *Eur. Polym. J.* **2012**, *48*, 1734–1744.

(44) Patel, A.; Mequanint, K., *Hydrogel Biomaterials*; IntechOpen 2011.

(45) Bardajee, G. R.; Hooshyar, Z. A novel biocompatible magnetic iron oxide nanoparticles/hydrogel based on poly (acrylic acid) grafted onto starch for controlled drug release. *J. Polym. Res.* **2013**, *20*, 298.

(46) Quintanilla de Stéfano, J. C.; Abundis-Correa, V.; Herrera-Flores, S. D.; Alvarez, A. J. pH-Sensitive Starch-Based Hydrogels: Synthesis and Effect of Molecular Components on Drug Release Behavior. *Polymers* **2020**, *12*, 1974.

(47) Behera, U. S.; Mishra, P. C.; Radhika, G. B. Optimization of multiple parameters for adsorption of arsenic (III) from aqueous solution using Psidium guajava leaf powder. *Water Sci. Technol.* **2022**, *85*, 515–534.

(48) Vijayaraghavan, K.; Palanivelu, K.; Velan, M. Biosorption of copper(II) and cobalt(II) from aqueous solutions by crab shell particles. *Bioresour. Technol.* **2006**, *97*, 1411–1419.

(49) Tang, S. C. N.; Wang, P.; Yin, K.; Lo, I. M. C. Synthesis and Application of Magnetic Hydrogel for Cr(VI) Removal from Contaminated Water. *Environ. Eng. Sci.* **2010**, *27*, 947–954.

(50) Ho, Y. S.; McKay, G. A Comparison of Chemisorption Kinetic Models Applied to Pollutant Removal on Various Sorbents. *Process Saf. Environ. Prot.* **1998**, *76*, 332–340.

(51) Zhang, Y.; Lin, S.; Han, M.; Su, Q.; Xia, L.; Hui, Z. Hui, Adsorption Properties of Magnetic Magnetite Nanoparticle for Coexistent Cr(VI) and Cu(II) in Mixed Solution. *Water* **2020**, *12*, 446.

(52) Ghaemy, M.; Sekhavat Pour, Z. Removal of dyes and heavy metal ions from water by magnetic hydrogel beads based on poly(vinyl alcohol)/carboxymethyl starch-g-poly(vinyl imidazole). *RSC Adv.* **2015**, *5*, 64106–64118.

(53) Wan, J.; Chen, L.; Li, Q.; Ye, Y.; Feng, X.; Zhou, A.; Long, X.; Xia, D.; Zhang, T. C. A novel hydrogel for highly efficient adsorption of Cu(II): synthesis, characterization, and mechanisms. *Environ. Sci. Pollut. Res.* **2020**, *27*, 26621–26630.

(54) Hassan, S.; Yasin, T.; Imran, Z.; Batool, S. Investigation of copper (Cu²⁺) adsorption performances and gamma radiation dose effect of polymeric hydrogel. *AIP Adv.* **2018**, *8*, No. 025301.

(55) Tian, R.; Liu, Q.; Zhang, W.; Zhang, Y. Preparation of Lignin-Based Hydrogel and Its Adsorption on Cu²⁺ Ions and Co²⁺ Ions in Wastewaters. *J. Inorg. Organomet. Polym. Mater.* **2018**, *28*, 2545–2553.

(56) Zhang, H.; Li, G.-W.; Feng, W.; Yao, Z.-Y. Cu(II) Adsorption from Aqueous Solution onto Poly(Acrylic Acid/Chestnut Shell Pigment) Hydrogel. *Water* **2022**, *14*, 3500.

(57) Pishnamazi, M.; Ghasemi, S.; Khosravi, A.; ZabihiSahebi, A.; Hasan-Zadeh, A.; Borghei, S. M. Removal of Cu (II) from industrial wastewater using poly (acrylamide-co-2-acrylamide-2-methyl propane sulfonic acid)/graphene oxide/sodium alginate hydrogel: Isotherm, kinetics, and optimization study. *J. Water Process. Eng.* **2021**, *42*, No. 102144.

(58) Chen, J.; Zhao, K.; Liu, L.; Gao, Y.; Zheng, L.; Liu, M. Modified kaolin hydrogel for Cu²⁺ adsorption. *e-Polymers* **2022**, *22*, 986–996.